Yet another face of Lorenz-Mie scattering:

Mono disperse distributions of spheres produce Lissajous like patterns

Alfons G. Hoekstra, [*] **Richard M.P. Doornbos,** [**]

Kirsten E.I. Deurloo, [**] **Herke Jan Noordmans,** [**]

Bart G. de Grooth, [**] **and Peter M.A. Sloot** [*]

[*]   Parallel Scientific Computing Group, department of Computer Systems, Faculty of

Mathematics and Computer Science, University of Amsterdam, Kruislaan 403, 1098 SJ

Amsterdam, the Netherlands, tel. (+31)20-5257463

[**]   Cell Characterization Group, department of TOP, Faculty of Applied Physics, University

of Twente, P.O. Box 217, 7500 AE Enschede, the Netherlands

Yet another face of Lorenz-Mie scattering:

Mono disperse distributions of spheres produce Lissajous like patterns

ABSTRACT

The complete scattering matrix S of spheres was measured in a FlowCytometer. The experimental equipment allows simultaneous detection of two scattering matrix elements for every sphere in the distribution. Two parameter scatterplots with x- and y- coordinates determined by the $S_{11} + S_{ij}$ and $S_{11} - S_{ij}$ values are measured. Samples of spheres with very narrow size distributions were analyzed with a FlowCytometer and produced unexpected two parameter scatterplots. Instead of compact distributions we observed Lissajous-like loops. Simulation of the scatterplots, using Lorenz-Mie theory, shows that these loops are not due to experimental errors, but due to true Lorenz-Mie scattering. We show that the loops originate from the sensitivity of the scattered field on the radius of the spheres. This work demonstrates that the interpretation of rare events and hidden features in FlowCytometry needs reconsideration.

KEY WORDS

Polarized light scattering, Mueller matrix, side scattering, FlowCytometry, two parameter scatterplot

1] INTRODUCTION

The problem of scattering of electromagnetic plane waves by an isotropic, homogeneous sphere of arbitrary size and refractive index was solved in 1890 by Lorenz.[1] Eighteen years later Mie, independent of Lorenz, arrived at the same, exact, analytical solution.[2] An excellent historical account of these important results can be found in the proceedings of the Ludvig V. Lorenz session of the Optical Particle Sizing conference 1990.[3] The mathematical richness of the formula is amazing and inspired many researchers to probe in still more detail the (differential) cross sections as a function of the radius or the refractive index of the sphere, or as a function of the wavelength of the incident light. The advent of modern computers and the development of efficient algorithms to calculate the complex functions appearing in the Lorenz-Mie scattering formula stimulated these efforts even more.

The Lorenz-Mie scattering formula posses some remarkable properties, most of which were demonstrated in scattering experiments. Well-known examples are the interference and ripple structure of the extinction cross section,[e.g. 4] glare points,[e.g. 5] or rainbows and glories.[e.g. 6,7] Despite the fact that the Lorenz-Mie solution is known for over a century, active research to the wealth of physically intriguing phenomena contained in Lorenz-Mie scattering continues. For instance, the internal electric field in the sphere receives more and more attention.[e.g. 8]

Lorenz-Mie scattering comes in many disguises. Thurn and Kiefer measured Raman spectra from optically levitated glass- and liquid spheres and observed a ripple structure superimposed on the bulk Raman spectrum.[9] The ripples proved to be due to structural resonances of the internal electric field, as could be demonstrated with the Lorenz-Mie theory. These structural resonance features could also be detected in stimulated Raman scattering from individual liquid droplets.[10] Tzeng et al. observed laser emission from small droplets at Lorenz-Mie resonance wavelengths.[11] These three effects are all due to the enhancement of the internal field intensity at a structural resonance.

This paper reports on yet another face of Lorenz-Mie scattering, which is based on the extreme sensitivity of the scattered field on the radius of the sphere. We measure the total

scattering matrix of spheres with a narrow size distribution ($\Delta r/r \sim 1\%$, with r the radius of the sphere) in a dedicated FlowCytometer (FCM). This experimental equipment allows us to measure $\mathbf{S}_{11}+\mathbf{S}_{ij}$ and $\mathbf{S}_{11}-\mathbf{S}_{ij}$ (ij = 12, 33, 34, $\mathbf{S}$ is the 4×4 scattering matrix) simultaneously for every single sphere in the distribution. FlowCytometry data is usually analyzed by generating a N-dimensional histogram (N being the number of observables per particle, here N = 2) from the experimental data and trying to identify different dataclusters in the histogram with different particles in the sample.[12] At first sight a distribution of homogeneous spheres with a very narrow Gaussian size distribution is expected to produce a single, narrow, Gaussian-like 2-dimensional histogram. However, it turned out that the measured histograms are all but Gaussian.

Here we will explain that this effect is <u>not</u> an experimental error, but due to true Lorenz-Mie scattering. We calculate the 2-dimensional histograms and obtain agreement between theory and experiment. In section 2 the theoretical and experimental background is shortly addressed, the results are presented in section 3 and discussed in section 4. Emphasis will be on the agreement between theory and experiment, but the consequences of this work for routine FCM experiments are also shortly pointed out. In section 5 conclusions are drawn.

2] MATERIALS AND METHODS

2.1 FlowCytometry

FlowCytometry[12] is an important technique in the biological sciences to identify and separate various populations of e.g. white bloodcells. Hydrodynamic focussing forces the cells to flow through a focussed laser beam one by one. Usually the cells are stained with fluorescent probes and the fluorescence of a cell in the laser beam is measured. Furthermore, the forward - and sideward scattered light is used as an important additional parameter for the analysis. In this way we can measure several fluorescence and elastic light scattering (ELS) signals for each cell in the sample.
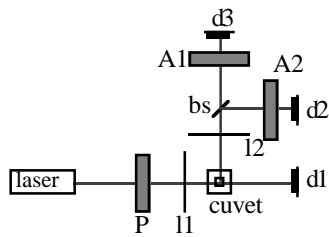
Figure 1: Schematic drawing of the optical system of the FlowCytometer. The laser beam is focussed by lens **l1** on a cell, flowing through the cuvet. The incident beam is polarized by means of the polarizer **P**. The intensity of the forward scattered light is measured by detector **d1**, the sideward scattered light is focussed by lens **l2** on detectors **d2** and **d3**, **bs** is a beamsplitter. The side scattering signals are passed through two different analyzers **A1** and **A2**.
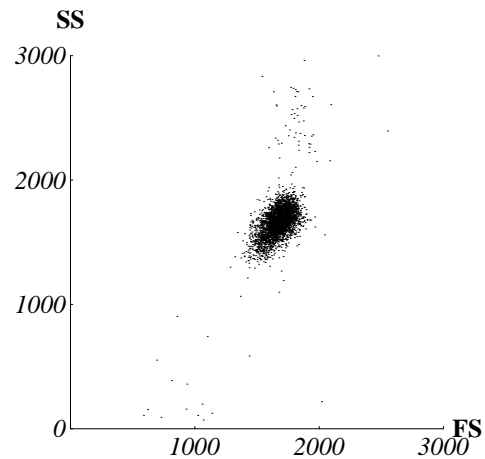

Figure 2: An example of a two parameter scatterplot for a large number of polystyrene spheres with a mean diameter of 1.98 μm, measured with a FlowCytometer. The wavelength was 0.6328 μm. Every dot represents a single sphere, the value of the x-coordinate is the intensity of the forward scattered light, the value of the y-coordinate is the intensity of the sideward scattered light. The intensities are in arbitrary units.

Sloot et al. argue that in many research- and clinical applications staining of cells is undesirable.[13] As a consequence a complete characterization of the sample must be obtained solely on the basis of ELS measurements. We expect that this is only possible by measuring suitable combinations of scattering matrix elements in the three principal FCM directions (forward-, sideward-, and backward scattered light).[13] The depolarization experiments of de Grooth et al.[14] to distinguish between neutrophilic- and eosinophilic granulocytes are a good illustration of this point.

We developed optics to measure the total scattering matrix in a FlowCytometer and showed that quantitative determination of the scattering matrix elements of particles in flow is possible.[13,15] The measuring principle was straightforward: a polarizer P was situated in the

4

incident beam and an analyzer A just before a detector in one of the principal directions. The matrix elements are obtained by measuring scattered intensities for various P-A combinations. We have extended the optics to allow simultaneous measurement of two P-A combinations in the side scattering direction, see figure 1.

A laser beam ($\lambda = 0.6328$ µm) is focussed by the circular lens l1 on the cells flowing through the cuvet, and polarized by the polarizer P. The beam waist radius in the focal point is 12.5 µm. After P the incident beam is either linearly of circularly polarized. The forward scattered light is detected by a silicon detector d1. Lens l2, a microscope objective (20 ×, NA = 0.4), collects the scattered light for $72.5° < \theta < 107.5°$, with θ the usual scattering angle. The sideward scattered light is divided in two beams by beamsplitter bs. The beams are directed onto different analyzers (A1 and A2) and the intensity after the analyzers is measured by the photomultipliers d2 and d3. The measuring principle is the same as described by Sloot et al.,[13] however here it is possible to measure a P-A1 and P-A2 combination for every single cell. This allows a direct measurement of single elements of the scattering matrix. Details of this equipment, and its application to measure the scattering matrix of white bloodcells will be published elsewhere.

2.2 Data handling

Our equipment measures three parameters for each cell: the forward scattered light and two P-A intensities in the sideward direction. The analog signals are digitized by 12 bit A/D converters and stored in memory of the controlling computer. In every run 4096 particles are measured, the results are stored on harddisk for off-line analysis.

The data are plotted in two parameter scatterplots in which each cell is represented by a dot in a x-y plot. The x- and y- coordinates are determined by one of the three measured parameters. Figure 2 gives an example of a scatterplot for polystyrene spheres with a mean diameter of 1.98 µm. The forward scattering is drawn along the x-axis and one side scattering signal is drawn along the y-axis. The spheres appear as a cloud of points in the scatterplot.

The shape of the data cloud in the scatterplots and the physical interpretation are the main

items of this paper.

2.3 Polystyrene spheres

The experiments were performed with polystyrene microspheres from Duke Scientific.* The diameters of the spheres are 1.98±0.05 μm, and 7.04±0.05 μm.

In addition to the diameter of the sphere, Lorenz-Mie calculations require the relative refractive index of the sphere. The refractive index of distiled water, in which the spheres are suspended, and polystyrene can be calculated from[16]

$$n_{water} = n_0 + \frac{n_2}{\lambda^2} + \frac{n_4}{\lambda^4} , \qquad\qquad [1]$$

with λ in micrometers, and $n_0 = 1.3236$, $n_2 = 3.35 \times 10^{-3}$, and $n_4 = -3.45 \times 10^{-5}$ for water, and $n_0 = 1.5711$, $n_2 = 4.82 \times 10^{-3}$, and $n_4 = 6.78 \times 10^{-4}$ for polystyrene. In our case $\lambda = 0.6328$ μm, which gives $n_{water} = 1.3318$ and $n_{polystyrene} = 1.5874$. In the calculations we will use

$$n_{relative} = n_{polystyrene} / n_{water} = 1.192,$$

and diameters as reported above.

2.4 Simulation of the scatterplots

To simulate the two parameter scatterplots the intensities measured by the sideward detectors must be calculated. For spheres, using the P-A combinations as described by Sloot et al., the intensity of the scattered light after analyzer A1 and A2 is[13]

$$I_A = I_0 C (\mathbf{S}_{11} \pm \mathbf{S}_{ij}), \; ij = 12, 33, \text{ or } 34, \qquad\qquad [2]$$

---

* Duke Scientific Polystyrene microspheres 1135D. San Antonio Palo Alto CA 94303

with I_0 the intensity of the laser beam, C an apparatus constant, and **S** the 4×4 scattering matrix of the sphere. The total intensity on the detector is obtained by integrating over the full solid angle $d\Omega$ defined by the field of view of the objective,

$$I_{det} = \int_{d\Omega} I_A \, d\omega = I_0 \, C \left[\int_{d\Omega} \mathbf{S}_{11} \, d\omega \pm \int_{d\Omega} \mathbf{S}_{ij} \, d\omega \right] \equiv I_0 \, C \left[\mathbf{s}_{11} \pm \mathbf{s}_{ij} \right], \qquad [3]$$

with $\mathbf{s}_{ij}$ an integrated matrix element.

To calculate the scattering matrix of a sphere in a focussed laser beam, the traditional Lorenz-Mie theory cannot be applied. Here we must rely on the generalized Lorenz-Mie theory which describes the scattering of a sphere in a Gaussian beam.[17] The $\mathbf{g}_n$ coefficients appearing in this theory are calculated using the localized interpretation.[18,19] We use the same programs as described in reference 13. The beamwaist radius of the Gaussian beam is 12.5 μm (see section 2.1). The particles are located in the focal point of the beam.

The procedure to generate a simulated scatterplot is as follows. First we calculate the scattering matrix $\mathbf{S}(\theta)$ as a function of the scattering angle θ (resolution $d\theta = 0.1°$) for a sphere with relative refractive index 1.192, diameter d, wavelength of the incident light 0.6328 μm, and the appropriate beamwaist diameter. Then the integrated scattering elements $\mathbf{s}_{ij}$ are calculated, as described in reference 13. The $\mathbf{s}_{ij}$ are calculated for 500 different values of d in the range

$$d_{mean} - 4\sigma_d \le d \le d_{mean} + 4\sigma_d , \qquad [4]$$

d_{mean} is the mean diameter in the distribution and σ_d the standard deviation (assuming a normal distribution in diameter). This results in arrays of $\mathbf{s}_{ij}(d_i)$, with discrete values d_i as defined above. For every d_i the $\mathbf{s}_{ij}(d_i)$ determine coordinates of a dot in the two parameter scatterplot, and the total scatterplot is generated by drawing dots for every value of d_i. To simulate the relative occurrence of spheres with diameter d_i in the distribution, the radius of the dots in the scatterplot is weighted with a Gaussian function:

7

$$r_{dot} = r_{max} \, Exp\left[-\frac{(d_i - d_m)^2}{2\sigma_d^2} \right],$$

[5]

r_{dot} is the radius of the dot for a sphere with diameter d_i, r_{max} is the maximum radius of dots in the simulated scatterplots.

2.5 Comparison between theory and experiment

The result of the calculations is a set $(s_{11}, s_{12}, s_{33}, s_{34})_i$, i runs over all the values of d. The measurements give arrays of detector signals, as in formula 3. We need an independent scaling for both theory and experiment in order to compare the two. The experimental results are scaled such that the apparatus constants I_0 and C are removed and the experimental scatterplots are entirely described in terms of scattering matrix elements. The scaling factor for the experimental results is

$$scale_{exp} = \frac{1}{2p} \sum_{i=1}^{p} (I_{A1}^i + I_{A2}^i) = \frac{1}{p} I_0 C \sum_{i=1}^{p} s_{11}^i,$$

[6]

with p the total number of measured spheres, and I_{A1} and I_{A2} the intensities of the scattered light after analyzer A1 and A2. Dividing the measurements by this factor results in two parameters for each measured sphere, independent of I_0 and C:

$$\left(\frac{1}{p} \sum_{i=1}^{p} s_{11}^i \right)^{-1} (s_{11} \pm s_{ij}).$$

[7]

These normalized experimental parameters are used as (x,y) coordinates in the scatterplots.

The term

$$\frac{1}{p}\sum_{i=1}^{p} \mathbf{s}_{11}^{i}$$

is the weighted mean $\mathbf{s}_{11}$ of the distribution of spheres. Assuming a normal distribution in diameter, this term is easily calculated from theory:

$$\overline{\mathbf{s}_{11}} = \int_{0}^{\infty} \frac{1}{\sigma_d \sqrt{2\pi}} \mathrm{Exp}\left[-\frac{(d - d_{mean})^2}{2\sigma_d^2}\right] \mathbf{s}_{11}(d)\, \delta d \ . \tag{8}$$

This integral is approximated by numerical evaluation for $d_{mean} - 4\sigma_d \le d \le d_{mean} + 4\sigma_d$, using Simpson's rule. The calculated integrated scattering matrix elements are divided by the value of this integral. After scaling, both theory and experiment can be compared. In the sequel of this paper the scatterplots of experimental and theoretical data are always scaled accordingly.

3] RESULTS

This section presents results of measurements and calculations of two parameter scatterplots of spheres. The normalized experimental and theoretical results are drawn in one figure. The x-axis always gives the $\mathbf{s}_{11}+\mathbf{s}_{ij}$ signal, and the y-axis the $\mathbf{s}_{11}-\mathbf{s}_{ij}$ signal, with ij as before. The dots in the theoretical curves are drawn according to equation 5. The small inset in the figures shows the theoretical curve once more, without scaling of the dot diameters.

Figure 3 shows the ($\mathbf{s}_{11}+\mathbf{s}_{12}$, $\mathbf{s}_{11}-\mathbf{s}_{12}$) scatterplot for the 7.04 μm spheres; the ($\mathbf{s}_{11}+\mathbf{s}_{33}$, $\mathbf{s}_{11}-\mathbf{s}_{33}$) and ($\mathbf{s}_{11}+\mathbf{s}_{34}$, $\mathbf{s}_{11}-\mathbf{s}_{34}$) scatterplot for this sample are drawn in figure 4 and 5 respectively. Finally the ($\mathbf{s}_{11}+\mathbf{s}_{12}$, $\mathbf{s}_{11}-\mathbf{s}_{12}$) scatterplot for the 1.98 μm spheres is drawn in figure 6.
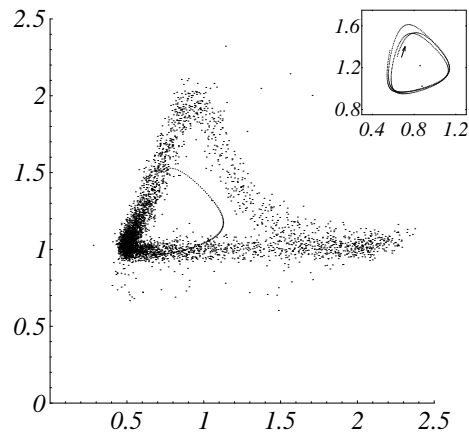
Figure 3: The normalized experimental and theoretical ($s_{11}+s_{12}$, $s_{11}-s_{12}$) scatterplot for polystyrene spheres with a mean diameter of 7.04 μm. The horizontal axes is the $s_{11}+s_{12}$ signal in the sideward direction, the vertical axes is the $s_{11}-s_{12}$ signal in the sideward direction. The inset shows the theoretical curve only, without scaling of the dot diameter. The arrow represents the starting point ($d_i = d_{mean} - 4\sigma_d$) and the loop direction, as d_i grows, of the theoretical curve.

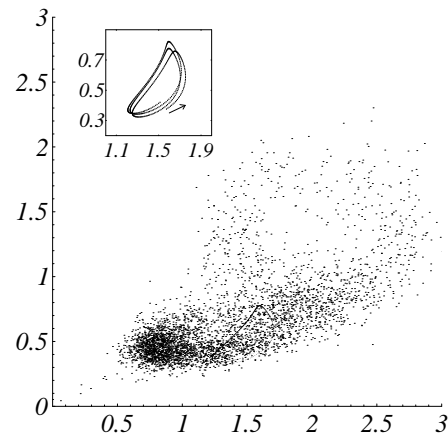Figure 4: Same as figure 3, but now for the ($s_{11}+s_{33}$, $s_{11}-s_{33}$) scatterplot.
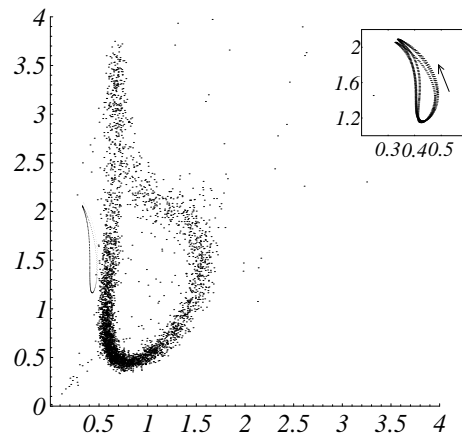
Figure 5: Same as figure 3, but now for the ($s_{11}+s_{34}$, $s_{11}-s_{34}$) scatterplot.
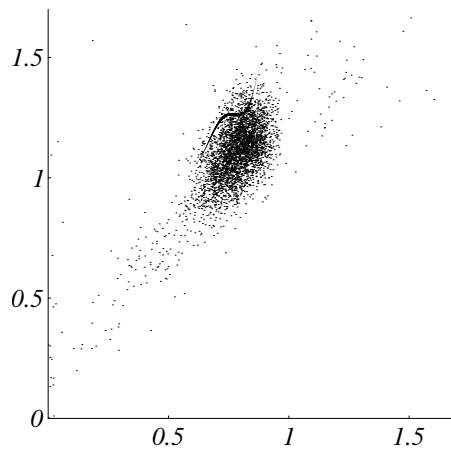

Figure 6: The normalized experimental and theoretical ($s_{11}+s_{12}$, $s_{11}-s_{12}$) scatterplot for polystyrene spheres with a mean diameter of 1.98 μm. The horizontal axes is the $s_{11}+s_{12}$ signal in the sideward direction, the vertical axes is the $s_{11}-s_{12}$ signal in the sideward direction.

4] DISCUSSION

Figures 3, 4, and 5 show the three normalized experimental and theoretical scatterplots for the 7.04 μm spheres. All three experimental scatterplots are loops, most obvious for the ($s_{11}+s_{12}$, $s_{11}-s_{12}$) and the ($s_{11}+s_{34}$, $s_{11}-s_{34}$) scatterplot.

The occurrence of loops in the scatterplots depends on the diameter of the spheres. Figure 6 is the ($s_{11}+s_{12}$, $s_{11}-s_{12}$) scatterplot for the 1.98 μm sphere. The experimental scatterplot is a

dense distribution of points, in agreement with the theoretical results. The same holds for the other two scatterplots. (data not shown).

The form and position of the normalized theoretical scatterplots for the 7.04 μm spheres compare very well with the experimental results. The agreement between theory and experiment for the $(\mathbf{s}_{11}+\mathbf{s}_{12}, \mathbf{s}_{11}-\mathbf{s}_{12})$ scatterplot is very good. The other two scatterplots only show a quantitative agreement between the theoretical and experimental results. Nevertheless, this demonstrates that the observed loops in the experimental plots are due to Lorenz-Mie scattering, and cannot be attributed to optical misalignments or other experimental errors.

Failure of a quantitative agreement between theory and experiment for the $(\mathbf{s}_{11}+\mathbf{s}_{34}, \mathbf{s}_{11}-\mathbf{s}_{34})$ scatterplot is probably due to the quality of the circular analyzers which are used to measure the $\mathbf{s}_{34}$ terms. Without going into details here, imperfect circular analyzers will cause a mixing of the $\mathbf{s}_{33}$ and $\mathbf{s}_{34}$ terms. This effect is still under investigation.

Theory and experiment can be compared on still another aspect. In the theory a normal distribution of spherical diameters was assumed, and this was simulated by weighting the radius of the dots in the scatterplot with a Gaussian function (see equation 5). The theoretical curves nicely show the distribution of the spherical diameter. However, as is obvious from the scatterplots for the 7.04 μm sphere, this distribution is in error with the experimental results. The experimental scatterplots have most points in the lower corner of the loops, whereas the theoretical results show that most points should show up along a long side of the loops. A closer look at the theoretical curves shows that this error between theory and experiment can be explained by assuming that the actual mean diameter of the spheres is somewhat larger than 7.04 μm, the value provided by the supplier of the spheres. The small inset in figures 3, 4, and 5 shows the theoretical curves, without scaling of the dot radius, and the starting point and loop direction of the curves. The starting point is for $d = d_{mean} - 4\sigma_d$, and for increasing diameter the curve loops in the direction of the arrow. The $(\mathbf{s}_{11}+\mathbf{s}_{12}, \mathbf{s}_{11}-\mathbf{s}_{12})$ scatterplot loops in clockwise direction, whereas the other two curves loop in counter clockwise direction. If the mean diameter of the sphere is increased, the position of the dots with large diameter in the theoretical curves shifts in the loop direction. Therefore, if the mean diameter of the sphere is increased to 7.08 μm, all three theoretical scatterplots reproduce the measured distribution correctly.

Furthermore, we measured the scatterplots for a slightly larger wavelength of the incident light ($\lambda = 0.647 \, \mu$m). In that case one expects that the same experimental loops occur, but with a small shift of the distribution of the data points in the loop. In all three scatterplots we observed this shift of the data points. The direction and magnitude of the shift are in agreement with calculated values (data not shown).

The origin of the loops in the scatterplots can be understood by examining the integrated matrix elements as a function of the diameter of the sphere. Figure 7 plots $\mathbf{s}_{11}$, $\mathbf{s}_{12}$, $\mathbf{s}_{33}$, and $\mathbf{s}_{34}$ as a function of the diameter of the sphere, for d as in equation 4, and d_{mean} is 7.04 μm. The matrix elements posses an extreme sensitivity on the diameter of the sphere. For 6.84 μm < d < 7.24 μm, $\mathbf{s}_{11}$ goes through three minima and maxima. The amplitude of the oscillations is approximately 20% of the mean value of $\mathbf{s}_{11}$. The other integrated scattering matrix elements have the same properties, although the oscillations are not in phase with the $\mathbf{s}_{11}$ oscillations. However, for spheres with 1.78 μm < d < 2.18 μm the $\mathbf{s}_{ij}$ elements increase monotonously with increasing d (data not shown).

In the diameter range of figure 7 the integrated scattering functions are almost periodic. The $\mathbf{s}_{11}$ strongly resembles a sine function. The other (quasi) periodic scattering matrix elements can be viewed as a Fourier series of sine and cosine functions. Fourier transformation of the data in figure 7 supports this view. For all four scattering matrix elements the absolute value of the Fourier transform peaks around the same ground frequency ν_0, and around higher harmonics $k\nu_0$ (with k an integer > 1). The amplitude of the third and higher harmonics are negligible compared to the amplitude of the ground frequency (data not shown).

When constructing the theoretical scatterplot, we actually draw a parametric plot, with the diameter of the sphere d as the only parameter. The functions on the x - and y-axes of the scatterplot are approximately combinations of sines and cosines of some ground frequency and higher harmonics. Therefore the scatterplots can be viewed as Lissajous plots. The oscillations in the integrated matrix elements, which are not in phase with each other, give rise to the Lissajous loops in the two parameter scatterplots. Note that in principle it is possible to measure more complicated scatterplots, with e.g. double loops (a ground frequency oscillation in one direction and a first harmonic oscillation in the other direction). Actually, in one instance we

measured scatterplots with such double loops. We are still working on the interpretation of these experiments.
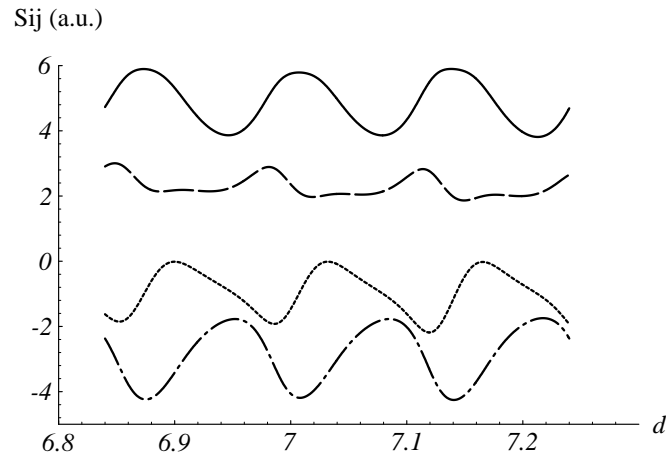
Sij (a.u.)

Figure 7: The integrated scattering matrix elements, as a function of the diameter d of the sphere; d is in micrometer, the s_{ij} are in arbitrary units; the solid line is s_{11}; the dotted line is s_{12}; the dashed line is s_{33}; the dashed-dotted line is s_{34}.

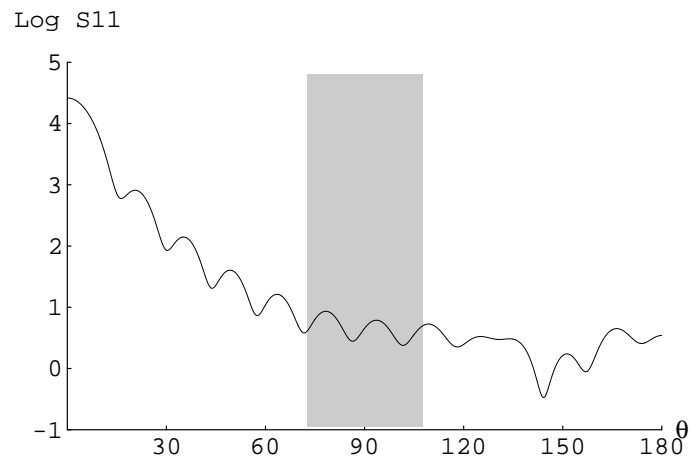Log S11

Figure 8: The S_{11} element as a function of the scattering angle θ, for d = 1.98 μm. The grey area denotes the field of view of the side scattering detectors.
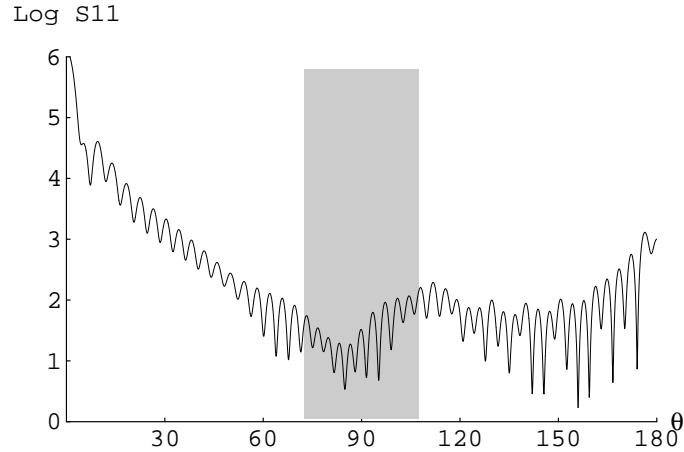
Figure 9: The S_{11} element as a function of the scattering angle θ, for d = 7.04 μm. The grey area denotes the field of view of the side scattering detectors.

Figures 8 and 9 show S_{11} as a function of the scattering angle θ, for d is 1.98 μm and 7.04 μm respectively. The grey area denotes the field of view of the side scattering detectors. If the diameter of the sphere is increased, the minima and maxima in $S_{11}(θ)$ gradually shift to the forward directions, and new minima and maxima seem to originate from θ = 180˚.[4] Slightly increasing the size of the 7.04 μm sphere results in entrance and exit of local minima and maxima in the field of view of the detectors, and changes in the amplitude of the minima and maxima, giving rise to the oscillations in the curves of the integrated matrix elements as a function of the diameter of the sphere (figure 7). The distance between the local minima and maxima in the $S_{11}(θ)$ curve for the 1.98 μm sphere is too large to induce strong oscillations in the integrated matrix elements after small changes of the diameter of the sphere.

Measurement of polarized light scattering in FCM is by no means a routine procedure yet, nevertheless our results contain an important warning. It is common practice in FCM to measure a side scattering signal. Since the incident light is always linearly polarized (most lasers emit light which is linearly polarized, perpendicular to the scattering plane), the intensity on the side scattering detectors is always a combination of s_{11} and s_{12}. Therefore a narrow monodisperse distribution of spheres can produce bimodal histograms in the side scattering channels (this can be seen in figure 3 for the $s_{11} + s_{12}$ signal). Especially if spheres are applied to calibrate the instrument, extra care should be taken, and small spheres should be used to

15

avoid the above mentioned problems. Furthermore, interpretation of rare events and hidden distributions in scatterplots requires careful analysis in view of the above mentioned effect. We are currently investigating to which extent the Lissajous loops can be expected in scatterplots from biological particles.

5] CONCLUSIONS

This report shows yet another face of Lorenz-Mie scattering; unexpected, Lissajous-like loops in two parameter scatterplots of spheres, as obtained by FlowCytometry. The complete scattering matrix of spheres, with a very narrow distribution in size, was measured with a dedicated FlowCytometer. The measured two parameter scatterplots can contain unexpected, Lissajous-like loops. By simulating these scatterplots, it was shown that the experimental results are true Lorenz-Mie scattering phenomena, and not due to experimental errors. The occurrence of loops in the scatterplots is dependent on the diameter of the spheres. It was shown that oscillations in the integrated matrix elements, as a function of the diameter of the sphere, form the basis for the Lissajous loops. These oscillations in their turn originate from the interference structure in the differential scattering cross sections.

A consequence of this behavior is the origin of bimodal histograms in the side scattering channels, due to monodisperse samples. This will hamper the interpretation of rare events and hidden distributions in the scatterplots.

6] ACKNOWLEDGEMENTS

7] REFERENCES

[1] L.V. Lorenz: Upon the light reflected and refracted by a transparant sphere. Vidensk. Selsk. Shrifter *6* (1890) 1-62.

[2] G. Mie: Considerations on the optics of turbid media, especially colloidal metal sols. Ann. d. Physik *25* (1908) 377-442.

[3] E.D. Hirleman (Ed). *Proceedings of the 2nd international congress on optical particle sizing*. Arizona State University Printing Services, March 1990 (part of the proceedings are published in the the 20 November 1990 issue of Applied Optics) .

[4] C.F. Bohren and D.R. Huffman: Absorption and Scattering of Light by Small Particles. John Wiley & Sons 1983.

[5] H.C. van de Hulst and R. Wang: Glare Point. Applied Optics *30* (1991) 4755-6763.

[6] R.T. Wang and H.C. van de Hulst: Rainbows: Mie computations and the Airy approximation. Applied Optics *30* (1991) 106-117.

[7] H.M. Nussenzveig: Complex angular momentum theory of the rainbow and the glory. J. Opt. Soc. Am. *69* (1979) 1068-1079.

[8] J.A. Lock: Interference enhancement of the internal fields at structural scattering resonances of a coated sphere. Applied Optics *29* (1990) 3180-3187.

[9] R. Thurn and W. Kiefer: Structural resonances observed in the Raman spectra of optically levitated liquid droplets. Applied Optics *24* (1985) 1515-1519.

[10] J.B. Snow, S.X. Qian, and R.K. Chang: Stimulated Raman scattering from individual water and ethanol droplets at morphology-dependent resonances. Optics Letters *10* (1985) 37-39.

[11] H.M. Tzeng, K.F. Wall, M.B. Long, and R.K. Chang: Laser emission from individual doplets at wavelengths corresponding to morphology-dependent resonances. Optics Letters *9* (1984) 499-501.

[12] M.A. van Dilla, P.N. Dean, O.D. Laerum, and M.R. Melamed: Flow Cytometry: Instrumentation and Data Analysis. Academic Press 1985.

[13] P.M.A. Sloot, A.G. Hoekstra, H. van der Liet, and C.G. Figdor: Scattering matrix elements of biological particles measured in a flow through system: theory and practice. Applied Optics *28* (1989) 1752-1762.

[14] B.G. Grooth, L.W.M.M. Terstappen, G.J. Puppels, and J. Greve: Light-Scattering Polarization Measurements as a New Parameter in Flow Cytometry. Cytometry *8* (1987) 539-544.

[15] P.M.A. Sloot and A.G. Hoekstra: Arbitrarily-shaped particles measured in flow through systems, in E.D. Hirleman (eds.)Proceedings of the 2nd international congress on optical particle sizing: . Vol. . 1990.

[16] E. Gulari: Latex particle size distributions from multiwavelength turbidity spectra. Part. Charact. *4* (1987) 96.

[17] G. Gouesbet, B. Maheu, and G. Grehan: Light scattering from a sphere arbitrarily located in a Gaussian beam, using a Bromwich formulation. J. Opt. Soc. Am. A *5* (1988) 1427-1443.

[18] G. Grehan, B. Maheu, and G. Gouesbet: Scattering of laser beams by Mie scatter centers:numerical results using a localized approximation. Applied Optics *25* (1986) 3539-3548.

[19] G. Gouesbet, G. Gréhan, and B. Maheu: Localized interpretation to compute all the coefficients g(n,m) in the generalized Lorenz-Mie theory. J. Opt. Soc. Am. A *7* (1990) 998-1007.